Stimulated electron energy loss and gain in an electron microscope without a pulsed electron gun

P. Das, J. D. Blazit, M. Tencé, L.F. Zagonel, Y. Auad, Y. H Lee, X. Y. Ling, A. Losquin, C. Colliex, O. Stephan, et al.

Stimulated electron energy loss and gain in an electron microscope without a pulsed electron gun

P. Das, J. D. Blazit, M. Tencé

Laboratoire de Physique des Solides, Université Paris-Sud, CNRS-UMR 8502, Orsay 91405, France

L. F. Zagonel, Y. Auad

"Gleb Wataghin" Institute of Physics, University of Campinas – UNICAMP 13083-859, Campinas, São Paulo, Brazil

Y. H. Lee, X. Y. Ling

Division of Chemistry and Biological Chemistry, School of Physical and Mathematical Sciences, Nanyang Technological University, Singapore 637371, Singapore

A. Losquin, C. Colliex, O. Stéphan

Laboratoire de Physique des Solides, Université Paris-Sud, CNRS-UMR 8502, Orsay 91405, France

F. J. García de Abajo

ICFO-Institut de Ciences Fotoniques, The Barcelona Institute of Science and Technology, 08860 Castelldefels (Barcelona) and ICREA-Institució Catalana de Recerca i Estudis Avancats, Passeig Lluis Companys, 23, 08010 Barcelona, Spain

M. Kociak

Laboratoire de Physique des Solides, Université Paris-Sud, CNRS-UMR 8502, Orsay 91405, France

Abstract

We report on a novel way of performing stimulated electron energy-loss and energy-gain spectroscopy (sEELS/sEEGS) experiments that does not require a pulsed gun. In this scheme, a regular scanning transmission electron microscope (STEM) equipped with a conventional continuous electron gun is fitted with a modified EELS detector and a light injector in the object chamber. The modification of the EELS detector allows one to expose the EELS camera during tunable time intervals that can be synchronized with nanosecond laser pulses hitting the sample, therefore allowing us to collect only those electrons that have interacted with the sample under light illumination. Using ~ 5 ns laser pulses of ~ 2 eV photon energy on various silver samples, we obtain evidence of sEELS/sEEGS through the emergence of up to two loss and gain peaks in the spectra at ± 2 and ± 4 eV. Because it does not involve any modification of the gun, our method retains the original performances of the microscope in terms of energy resolution and spectral imaging with and without light injection. Compared to pulsed-gun techniques, our method is mainly limited to a perturbative regime (typically no more that one gain event per incident electron), which allows us to observe resonant effects, in particular when the plasmon energy of a silver nanostructure matches the laser photon energy. In this situation, both EELS and EEGS signals are enhanced in proportion to $n + 1$ and n, respectively, where n is the average plasmon population due to the external illumination. The n term is associated with stimulated loss and gain processes, and the term of 1 corresponds to conventional (spontaneous) loss. The EELS part of the spectrum is therefore an incoherent superposition of spontaneous and stimulated EEL events. This is confirmed by a proper quantum-mechanical description of the electron/light/plasmon incorporating light-plasmon and plasmon-electron interactions, as well as inelastic plasmon decay.

Keywords: electron energy gain

1. Introduction

The three scientists honored in this special issue, one of them being an author of this article, have shared many common interests in electron microscopy and contributed with pioneering advances. They encompass in particular inelastic scattering, coherence, various sorts of fields mapping, the search for new electron-based techniques and the development of innovative instrumentation. It is therefore no surprise that we decided to present a new instrumental development in a relatively new field of electron microscopy mixing inelastic scattering of electrons and the influence of electromagnetic optical fields in an electron microscope, namely stimulated electron energy-loss spectroscopy (sEELS) and stimulated electron energy-gain spectroscopy (sEEGS).

The idea of shining a light beam onto a sample of interest and observing sEELS/sEEGS was prophesied by Archie Howie in a short proceeding for a conference (1). In that paper, he was screening some potential techniques able to help analyzing defects in semi-conductors, including photoelectron emission microscopy (PEEM), cathodoluminescence (CL) and emission of light by scanning tunneling microscopy. Interestingly, among all these techniques, only cathodoluminescence proved to be reliable for single-defect detection. In particular, point defects behaving as single photon emitters can now be detected (2; 3). Nevertheless, the other techniques found impressive applications in nanophotonics. In particular, Howie pointed out how PEEM could be utilized for plasmon mapping, and later it was brought to produce high resolution plasmon maps (4; 5) and ultrafast plasmon dynamics (6; 5). Archie Howie also discussed tip-enhanced Raman scattering (TERS), which can now image submolecular features with a Raman signal (7).

However, Howie's most striking prophecy was about electron energy gain. At the time, electron energy gains had been already detected several decades earlier in different configurations. Those include thermal EEGS, where electrons are accelerated by thermal phonons, detected almost 50 years ago with no spatial resolution (8; 9) - thermal EEGS can now be acquired with nanometer resolution (10). Acceleration of electrons with non-thermally excited quasi-particles (i. e., not phonons, but rather higher energy quasi-particles such as for example plasmons) has also been proved a long time ago: Schilling and Raether (11) managed to observe EEGS from high-energy plasmons using an high-intensity electron beam; with such a beam, the incoming electrons pump the system, so that trailing electrons in the same beam could pick up the energy deposited by leading electrons and be accelerated. Also, acceleration of electron beams with a light beam was discussed in the context of the inverse Cerenchov effect (12). But Howie predicted a brand new physical mechanism of electron energy gain, namely, the acceleration of electrons by the field scattered by nanoscale objects illuminated by a laser beam (1).

Almost ten years later, two of us calculated the probability for an electron to be accelerated close to a plasmonic nanoparticle (13), showing that it could be possible to see a peak in the gain part of the EELS spectrum using reasonably high-power continuous-wave (CW) laser light.

The electron energy-gain spectroscopy (EEGS) proposed in Ref. (13) was concerned with resonant structures excited by light and probed at the nanometer scale. This work focused on the increase in spectral resolution, which could be only limited by the laser spectral width, and not by the zero-loss-peak (ZLP) energy width of the electron microscope, which is orders of magnitude higher. The principle of electron energy gain in laser-excited samples was experimentally demonstrated one year later by Barwick and collaborators (14). In contrast to the perturbative regime that we studied (13), the effect demonstrated in the experiment conducted by the group of the late Ahmed Zewail was not a small perturbation, but led to a spectrum overwhelmed by replicas, with multiple peaks spaced by the exciting laser energy, on the gain and loss parts of the spectrum in a nearly symmetric distribution relative to the ZLP. Indeed, the experiment was performed using a femtosecond pulsed laser able to both trigger electron emission and sample light irradiation. With proper synchronization, the overlap between the electron and laser pulses could be made sufficiently large to make the intensity of the replica peaks similar to that of the ZLP. Using this high signal-to-noise ratio spectra, images of the electromagnetic field scattered by the nano-object could be resolved. Such microscopy technique was therefore baptized as photon-induced near-field electron microscopy (PINEM). The occurrence of the multiple replicas occurring in PINEM was soon described theoretically (15). PINEM was further used to map electromagnetic fields of various structures, including surface plasmons polaritons

(16). It was also recently extended to tunable femtosecond lasers, allowing spectrally resolved plasmon imaging to be performed (17).

In Ref. (15), the special case in which the photon pulse is much longer than the electron pulse was also analyzed, showing even stronger effects, including a vanishing of the ZLP and quantum-billiard transitions between spectral peaks associated with different net numbers of exchanged photons. These effects were brilliantly demonstrated in 2015 by Feist and collaborators (18), who interpreted the results in terms of Rabi oscillations of the fast electron between the free propagation eigenstates shifted by multiples of the laser excitation. We note that Feist et al. used an ultrafast high-brightness/high-coherence gun (a Schottky field emission gun in this case) in order to be able to observe this effect with high spatial resolution (note that similar effects can be retrieved without spatial resolution with a low brightness gun (19)). More generally, the use of a high coherence gun should be a pre-requisite for both time-resolved holography and spatially resolved analytic microscopy (20). For spectroscopic works at high spatial resolution, as the one of the present paper, high brightness indeed allows to get high current densities for incident angles small enough such as not inducing spatial resolution degradation due to geometrical aberrations.

Now, the development of a high-brightness pulsed electron gun is a demanding task (21). Switching between continuous and pulsed configurations through the electron gun is usually not easy. Additionally, changing the gun in an existing microscope involves a complex and costly effort. Therefore, one may wonder if a more versatile and cheaper solution is possible. On a more fundamental level, one may also want to explore a simpler physical configuration, in which the interaction between the electron and the photon, as mediated by a nano-object, is essentially linear, and where the spectral resolution in the sEELS/sEEGS spectra is closer to that used in regular EELS for nano-optics, which is significantly higher than the one currently reported in pulsed-gun-technology studies. In this way, gain *spectroscopy*, which has been elusive until now, could be made possible.

In this paper, we present a technique in which, instead of exciting a sample with synchronized sub-picosecond pulsed electron and laser beams (pulsed excitation technique), we are irradiating the sample with a stochastic electron beam and a pulsed laser, the later synchronized with the detection (pulsed detection technique). In the pulsed excitation technique, all electrons have the possibility to experience stimulated gain or loss and then contribute to the collected spectrum. In the pulsed detection technique that we introduce here, most of the electrons do not experience sEEL and sEEG, and therefore only inelastic events arising when the sample is exposed to the laser have to be detected through synchronized detection. We show that indeed sEELS/sEEGS replicas can be observed in this way. We report a spectral resolution better than 500 meV, as measured by the full width at maximum (FWHM) of the ZLP. Compared to the pulsed excitation technique, the pulsed detection approach shows sEELS/sEEGS peak intensities that are approximately linear with the laser intensity. We then demonstrate the possibility to perform spectral imaging interchangeably with and without sEELS/sEEGS signals. By working with a nanostructure exhibiting a mode in resonance with the incident laser, we could further unveil basic properties of resonant sEELS/sEEGS. First, compared to the off-resonance situation probed in the same experiment, sEELS/sEEGS peaks are largely enhanced due to the resonant matching of the laser and the structure mode energy. Additionally, the EELS peak intensity is higher than its EEGS counterpart. As confirmed by a detailed theoretical treatment presented below, this discrepancy with the current literature can be simply explained by the fact that in our case loss and gain events should be proportional to $n + 1$ and n, respectively, where n is the average number of plasmons created by the incident laser. This dependence describes the probability of creating and destroying a bosonic plasmon mode, with the term n being associated to stimulated loss and gain processes, respectively, and the term of 1 representing spontaneous losses (i.e., conventional EELS). The EELS events are therefore incoherent superpositions of spontaneous and stimulated EEL ones.

2. Experimental details

The principle of a pulsed-detection sEELS/sEEGS setup is given in Figure 1, together with a timeline in Figure 2. A conventional (S)TEM (a dedicated VG HB501 in this paper) is fitted with a light injection device (based on the Attolight Mönch 4107 in the present case) through which a laser beam can be focused on the sample. The

microscope is also fitted with a modified EELS spectrometer and detector. The main modification of the EELS detection scheme is the addition of a fast deflector after the last quadrupole of a modified 666 Gatan spectrometer. Combined with a slit in front of the scintillator, the deflector allows us to periodically obtain a stationary beam hitting the scintillator during a customizable period as short as $\tau_{ON} = 18\,\text{ns}$ (ON time). In the present case, the deflection period is chosen to match the repetition rate $R = 1/\tau_R = 10\,\text{kHz}$ of a nanosecond-pulse high-power SYRAH Credo laser. This laser emits 582 nm (2.13 eV) pulses of $\delta = 5\,\text{ns}$ duration. We usually set τ_{ON} to its minimum (i.e, as close as possible to the value of δ) and adjust the delay Δ between the laser and deflector pulses so that all the electrons that have been emitted during the period in which the sample was irradiated by the laser are finally detected (see Figure 2). The setup is prepared to send an average power tunable between 0 and more than 400 mW after coupling into an optical fiber. Using an optical fiber simplifies alignments at the price of reducing the maximum power density achievable. If needed, however, nothing prevents the experiment from being made free-space with the light injection system used (21). We used a field programmable gate array (FPGA) for synchronization electronics to synchronize the triggering of the laser emission and the beam deflection. The delay Δ between the two of them can be fine-tuned with a programmable 5 ns precision. EELS spectra, or more generally EELS, sEELS and sEEGS spectra, are acquired on a Princeton proEM electron multiplying charge coupled device (EMCCD) camera, and simultaneously, high-angle-annular-dark-field (HAADF) data can also be detected. The EMCCD camera was used in its low-noise mode (non-EM mode, similar to a regular CCD camera). For the remaining of this article, we used 15 mrd incidence and acceptance angles, and a typical current of 50 pA in the probe.

A very important point in the present setup is that the operation of the microscope is exactly the same as a regular one, even if of course the sample can be affected physically by the laser illumination (see below). For example, for electron dose sensitive sample, a regular pre-specimen blanker (with μs resolution in our setup) can be synchronized with the end of the ON time. The probe stability is not affected by the illumination, and the HAADF imaging is only slightly perturbed by stray light coming from the laser. The stray light is due to the design of the VG microscope, where no electron optics exists between the sample and the HAADF detector to protect the later. However, it would be naturally screened from light in a more modern microscope. Additionally, it is important to note that the EELS detection system is not affected by our pulsed detection approach. Indeed, pulsed detection does not induce extra aberrations in the spectrometer, as it stands after all the electron optics (see a demonstration below). EELS spectra are acquired with typically millisecond to seconds dwell time, during which an arbitrary number N of light pulses and ON deflector times take place (see Figure 2). This means that typically $N = 10$ to $N = 10^4$ pulses have interacted during the dwell time. Apart from the fact that the effective current reaching the EELS camera is reduced by a factor $10^4 \times 5 \times 10^{-9} = 5 \times 10^{-5}$ (the accumulated time during which the signal reaches the detector in one second is the repetition rate multiplied by the pulse width), the EELS detector works the same way as without pulsed operation. Therefore, spectral and HAADF imaging can transparently be performed in the pulsed or non-pulsed configurations with no modification of the setup, which is a practical major advantage over the regular, pulsed-gun configuration.

For light injection alignments, we usually first prealigned the light injector to maximize the cathodoluminescence signal. Then, we brought the laser power to a point where holes could be drilled in some sacrificial part of the sample and realign this way, if necessary.

3. Results and discussion

Samples were prepared by Joule-evaporating a 250 nm thick silver film on top of a regular TEM carbon holey grid. Silver nanocubes in solution were further deposited. In many places the cubes could stick out in a hole, yet being in thermal contact with the film. This allows us to collect a substantial sEELS/sEEGS signature without melting the sample.

Figure 3 shows a proof-of-principle of sEELS/sEEGS acquired with the beam positioned in the vacuum next to a folded piece of silver film. A clear sEELS/sEEGS signature is observed, revealing the presence of peaks at multiples of the photon energy. In this particular instance, two sEELS and two sEEGS peaks (replicas) could be resolved. However, in most cases, the power

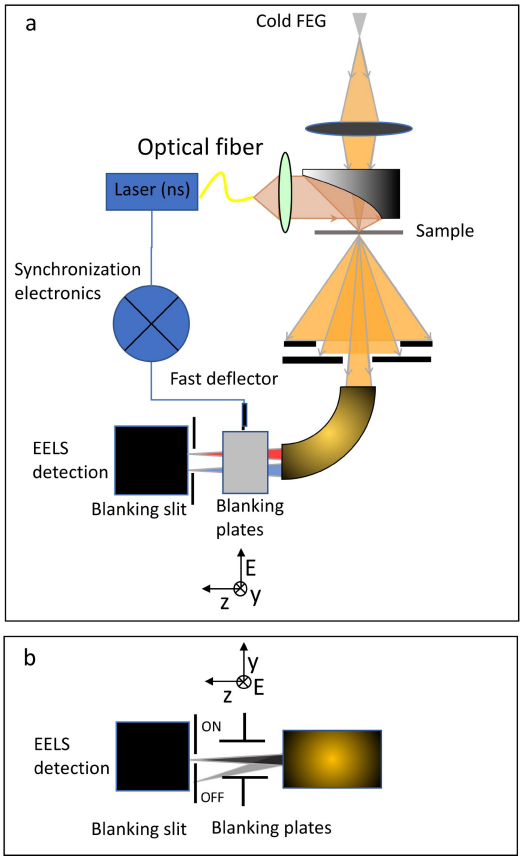

Figure 1: Schematics of the pulsed-detection sEELS/sEEGS setup. The scanning coils and spectral-imaging electronics are omitted for clarity. a. Side view including the dispersive axis (E). b. bottom view including the non-dispersive axis (y).

needed to observe the replicas (here around 432 mW or 6.35×10^{14} W/m^2, as determined by the modelization of the light injection configuration) led to the destruction of the sample. Even in the present extreme case, we note that only two replicas could be observed, with a maximum intensity (area under the peak) of $\approx$ 20% of the ZLP. This is much smaller than what is usually observed in pulsed-gun sEELS/sEEGS experiments (14; 16; 18), where the interaction can be so strong that the ZLP eventually drops to zero (18). In our pulsed-detection measurements, the sEELS/sEEGS signal is generally of the order of the regular EELS signal from plasmons in large nanoparticles (i.e., a fraction $\sim 10^{-3} - 10^{-2}$ of the ZLP).

We present in Figure 4 the effect of changing the delay between the laser pulse and the fast deflector pulse. In this case, we set $\tau_{ON} = 28$ ns. We see that the signal drops to zero within ± 10 ns. This is slightly smaller than expected from the overlap of the ON time and laser pulse duration, possibly because of an effective ON time shorter than expected. We are currently investigating this effect.

Knowing that the observed signal corresponds indeed to sEELS/sEEGS, we turn our attention to a few differences with respect to the pulsed-gun technology. Figure 5 presents a sEELS/sEEGS spectrum acquired close to a silver nanocube. The FWHM of the ZLP and the replicas is slightly smaller than 0.5 eV. This is very close to the nominal value of the FWHM of the ZLP on this microscope, as seen from the overlapped ZLP obtained under regular conditions in Figure 5. The main limits in this particular microscope stem from the lack of stability of the high acceleration voltage and spectrometer power supplies, the quality of the scintillator and the relatively high incidence and acceptance angles (and related aberrations) used here. A modern microscope and spectrometer combination typically reach better than 300 meV on a routine basis, see e. g. (22). This is in contrast to the pulsed-gun approach, which is currently limited above 600 meV (20; 23), owing in part to energy broadening due to the electrons photoemission physics and in part to the stability of the electron microscope and spectrometer. We understand that there is no reason to expect that our type of setup could not be implemented in a monochromated electron microscope and reach state-of-the-art spectral resolution (currently in the sub-10 meV range (24)). A second aspect that appears as a striking difference with respect to the pulsed-gun sEELS/sEEGS

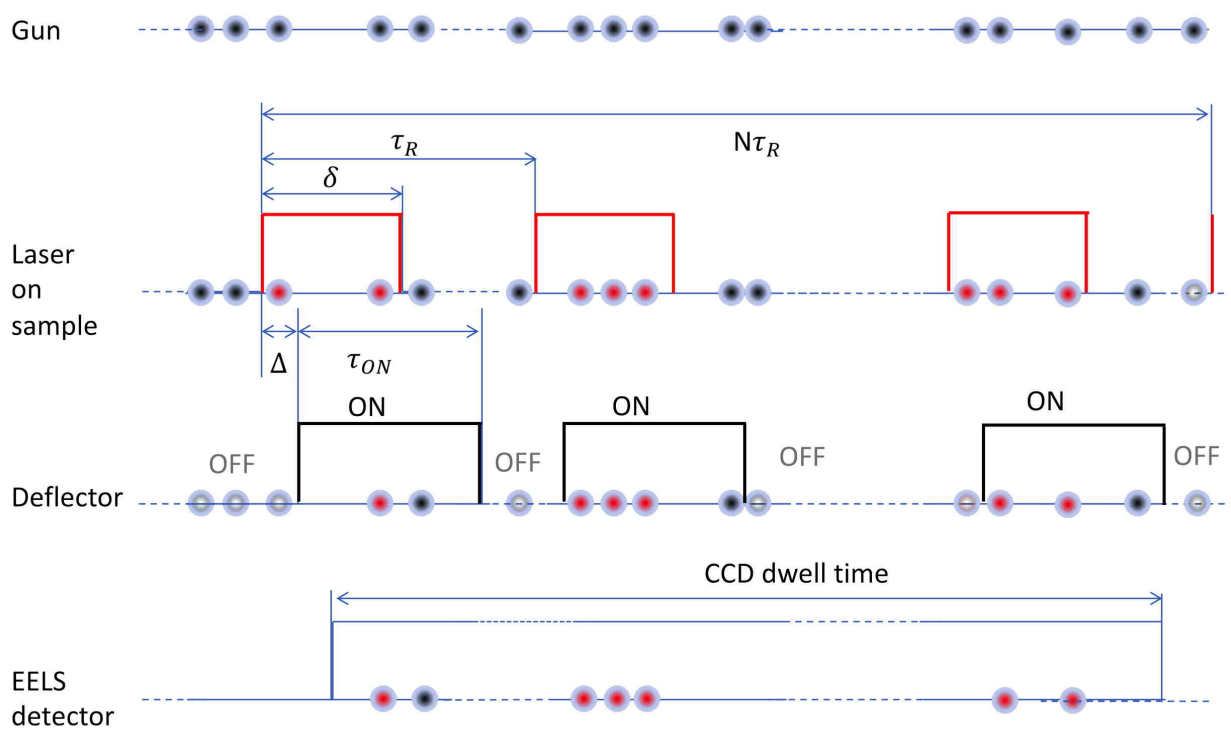

Figure 2: Synchronization scheme of the pulsed detection. From top to bottom, we indicate the relevant elements in the electron column of Figure 1. Note that the photon pulses and electron deflection shapes have been schematized as rectangular gate functions.

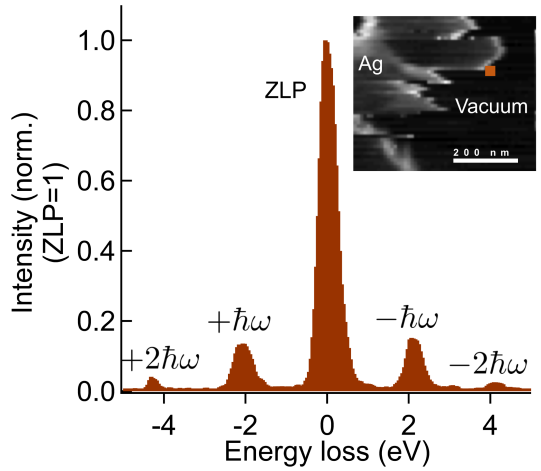

Figure 3: Proof-of-principle pulsed-detection sEELS/sEEGS with two replicas. The data have been collected with the beam position fixed close to a thick silver layer (see inset) with a laser power density of 6.35×10^{14} W/m^2 and an acquisition time of 1 s.

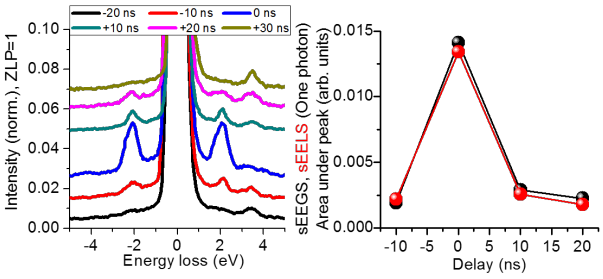

Figure 4: Effect of the delay between laser excitation and fast deflection. The electron beam is placed close to a melted part of a silver film Left: series of spectra taken at various delays, as indicated in the legend. The dwell time is 1000 ms, the detection ON time τ_{ON} is 28 ns. A total of 20 spectra have been acquired in this configuration, realigned with respect to their ZLP position and averaged. Right: Integrated intensity of the first replica (EEGS and EELS) as a function of delay. The integrated intensity has been calculated by removing a linear background contribution, then summing the intensity under each of the peaks.

technologies is the linearity of the phenomenon in our pulsed-detection scheme. More precisely, as exemplified in Figure 6, the intensity of a replica scales linearly with the injected power. Although pulsed-gun setups can of course be operated in this regime, they are commonly used in a strong nonlinear regime in which the summed sEEGS is larger than the ZLP, leading to an excellent signal to noise ratio for application in e.g. PINEM. In our case, trying to reach a nonlinear regime leads to destruction of our samples, due to the necessary much higher power. The quality of the data in the pulsed-detection scheme, where the sEELS/sEEGS signal is of the order of magnitude of the regular EELS signal, i.e several order of magnitudes smaller than a typical PINEM signal, relies therefore on the same optimization of the detection setup as in conventional EELS (25).

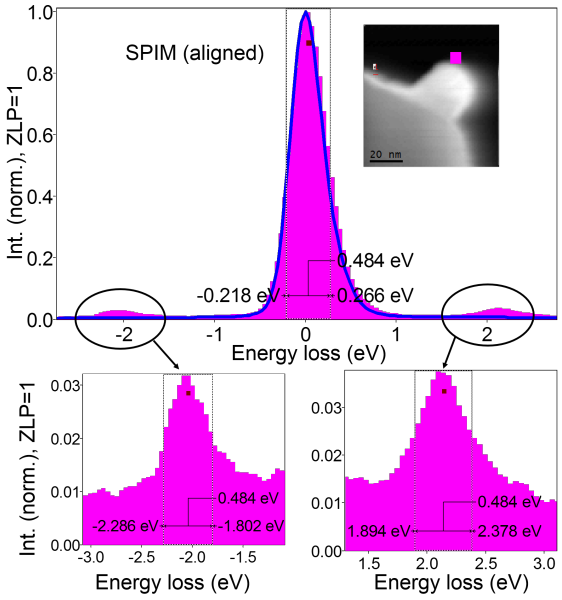

Figure 5: Typical spectrum extracted from spectral imaging performed on a silver nanocube (see Figure 7). In the pulsed-detection mode (magenta spectrum), the ZLP as well as the replicas have a FWHM slightly smaller than 0.5 eV. A spectrum obtained in regular mode (blue) is also shown for comparison.

We next turn our attention to the study of resonant sEELS/sEEGS signals. In the preceding examples, point spectra were taken at positions relevant to unveil the main properties of the pulsed-detection sEELS/sEEGS

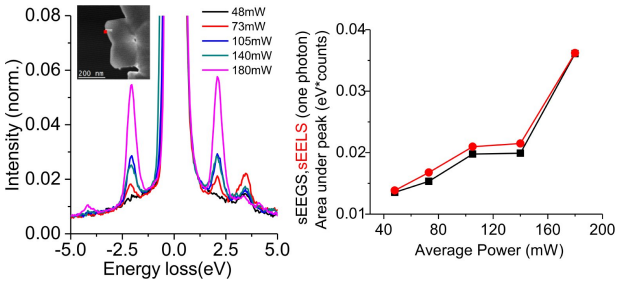

Figure 6: sEELS/sEEGS experiments in the linear regime. Left: spectra measured with an electron beam close to coalescent silver nanocubes (see inset) for various laser powers. Right: area under the sEEGS and sEELS first replica peaks as a function of laser power, showing an approximately linear dependence.

approach. We selected points where the laser energy was not matching any resonance of the system. In order to study the effect of resonantly exciting a plasmon mode, we performed regular EELS spectral-imaging on a silver nanocube lying attached to a silver film edge with part of it on the vacuum side, as shown in Figure 7 (top inset). In this spectral image, the laser was left on, but the ON state of the deflector was set to 9000 ns, much larger than the 10 ms acquisition dwell time of individual spectra. This way, the obtained EELS spectra were directly comparable with the pulsed-detection mode (i.e., the sample was irradiated the same way). The spectra of this object, which have been normalized to the total number of counts in order to quantitatively compare the signals in both configurations, present two major features, one at ≈2 eV and localized on the suspended part of the cube, and another one at ≈3.2 eV on the film side, as shown in the filtered maps of the inset to Figure 7 (top). Although the sample was irradiated by a laser beam, no sEELS/sEEGS signal was detected, because it was overwhelmed by the ZLP and the regular EELS signal originating from the time periods in which the sample was not illuminated (i.e., most of the time due to the large ON state of the deflector). As already mentioned above, triggering the pulse detection operation does not affect the overall performance of the microscope, which makes it easy to compare regular EELS and sEELS/sEEGS signals in spectral-imaging mode. We therefore performed a second spectral image in a pulsed-detection mode where the ON time (18 ns) was slightly larger than the laser pulse duration. The results are displayed in Figure 7 (bottom). A spectrum taken close to the film exhibits the ≈3.2 eV mode, in addition to a small sEELS/sEEGS signal at the laser energy. The filtered map at this energy (not shown) is quite comparable to that of Figure 7 (top). The only noticeable difference lies in the signal-to-noise ratio, which is obviously much worse in the sEELS/sEEGS mode, an effect that we attribute to the $\approx\ 5\times10^{-4}$ drop in the signal reaching the EELS detector (everything else being equal) in the pulsed detection mode (i.e., the small fraction of time in which the detector is ON). The situation is quite different for the ≈2 eV plasmon peak, which is nearly in resonance with the laser injection (i.e., the energy difference between plasmon and incident photon energies is 0.13 eV, which is small compared with the FWHM of the plasmon). First, the sEELS/sEEGS signal is now largely enhanced to the point that it is much larger than the ≈3.2 eV signal or the EELS signal of the ≈2 eV plasmon peak. Second, the sEELS and sEEGS maps, despite the noise, closely resemble each other. However, they slightly differ from their EELS counterpart. The signal is now more localized on the two tips of the cube, which is a characteristic difference between EELS and sEELS/sEEGS (see theoretical description below). Finally, the spectral weight of the sEELS and sEEGS spectra are clearly different. This is in stark contrast with the available experimental literature, in which sEELS/sEEGS replicas are totally symmetric.

4. Theoretical description

We can obtain insight into the electron/light/plasmon interaction processes through a proper quantum-mechanical description incorporating light-plasmon and plasmon-electron interactions, as well as inelastic plasmon decay, taking into account that light and electrons cannot directly interact due to their energy-momentum mismatch. We thus write the Hamiltonian of the system as

$$\begin{aligned}\mathcal{H} =&\hbar\omega_{\mathrm{p}}\, a^{\dagger}a+\hbar\sum_{k}\varepsilon_{k}b_{k}^{\dagger}b_{k} \\ &+g(t)\left(a^{\dagger}+a\right)+\sum_{kk'}\left(g_{kk'}b_{k}^{\dagger}b_{k'}a+g_{kk'}^{*}b_{k'}^{\dagger}b_{k}a^{\dagger}\right),\end{aligned} \tag{1}$$

where $a^{\dagger}$ and a represent creation and annihilation operators of the plasmon, respectively, $b_k^{\dagger}$ and b_k create and

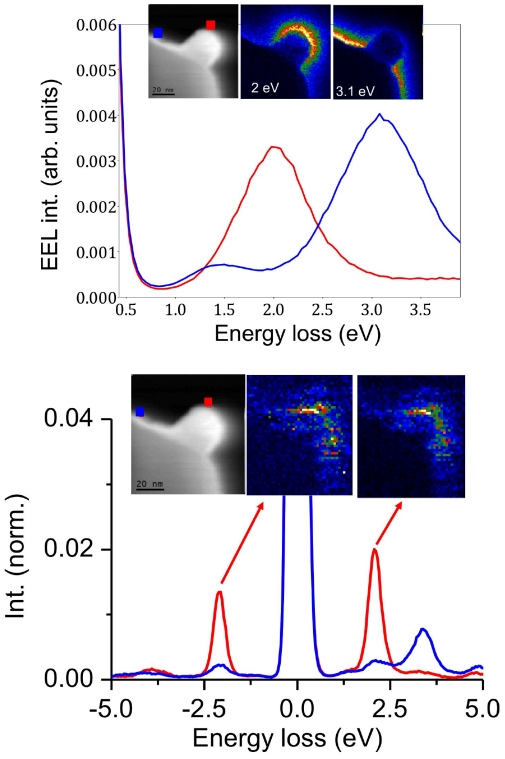

Figure 7: sEELS/sEEGS spectral-imaging experiments in the resonant regime. The laser power is 73 mW ($\approx 10^{14}$ W/m^2). Top: EELS spectral-imaging with 900 ms ON time. In this configuration, the sample is illuminated, but most of the detected electrons do not undergo any sEELS/sEEGS event. Inset: HAADF image of the structure (colored squares indicate the position of the beam where the spectra of corresponding colors in the main panel have been acquired) and filtered images for two main modes. Bottom: sEELS/sEEGS spectral-imaging with shorter ON time. Specifically, the ON time is close to the laser pulse duration, leading to a clear observation of sEELS/sEEGS features. Inset: HAADF image of the structure (colored squares indicate the position of the beam where the spectra of corresponding colors in the main panel have been acquired) and filtered images around the energies of the sEELS/sEEGS first peak.

annihilate an electron of wave vector k and kinetic energy $\hbar\varepsilon_k$ along the beam direction, and ω_p is the plasmon frequency. Terms in the first line of eq. (1) describe the non-interacting plasmon and electron, respectively, whereas the second line incorporates interaction terms. In particular, the externally applied light of frequency ω_0, approximated to be continuous wave, interacts with the plasmon through a time-varying rate $g(t) = 2\mathrm{Re}\left\{g_0 \mathrm{e}^{-\mathrm{i}\omega_0 t}\right\}$, where $g_0 = -\mathbf{E}_0 \cdot \mathbf{p}$ is written in terms of the optical electric field amplitude $\mathbf{E}_0$ and an effective plasmon dipole $\mathbf{p}$. For simplicity, we assume in what follows a single plasmon mode.

Before we discuss the effect of inelastic decay of the plasmon, we can examine the Hamiltonian (1) to extract some general characteristics of the electron spectrum. Assuming the initial state to contain n plasmons (i.e., a plasmon Fock state $|n\rangle$) and neglecting light-plasmon interaction during the passage of the electron, we can use the Fermi golden rule to first order in the electron-plasmon interaction $g_{kk'}$ to find that the electron spectrum contains two peaks separated by energies $\pm\hbar\omega_\mathrm{p}$ from the ZLP, whose magnitudes are proportional to $n+1$ and n in the loss and gain peaks associated with matrix elements for transitions to plasmon states $|n+1\rangle$ and $|n-1\rangle$, respectively. The loss peak is therefore more intense than the gain peak (in agreement with experiment), as both of them contain a term proportional to the plasmon population n (stimulated process), but the loss peak has an additional term $(+1)$ representing spontaneous (i.e., conventional) loss events. We thus conclude that direct comparison between loss and gain peaks in the measured spectra allows us to determine the number of plasmons n continuously excited by the external illumination before arrival of the electron, as the peak ratio is simply given by $(n+1)/n$. In the case of Figure 7, for example, the comparison of the area under the gain and loss peaks in the illuminated and non-illuminated case gives an average number of plasmon of $n \approx 1.2$, in agreement with the linear regime reached in the present experiments. We note that this value is slightly underestimated, as the ON time is larger than the δ time, therefore there are more spontaneous events counted arising during the time where the electrons are detected but the laser is not illuminating the sample.

4.1. Inelastic plasmon losses

In a realistic scenario, plasmons have a finite lifetime that affects the profile of the resulting electron spectrum. We introduce this effect through a finite plasmon decay rate γ by resorting to the density matrix of the system ρ, which is subject to the equation of motion

$$\frac{d\rho}{dt} = \frac{\mathrm{i}}{\hbar}[\rho, \mathcal{H}] + \frac{\gamma}{2}\left(2a\rho a^\dagger - a^\dagger a\rho - \rho a^\dagger a\right). \quad (2)$$

It is then convenient to express the density matrix in the interaction picture as

$$\rho = \sum_{ll'}\sum_{kk'} \alpha_{ll',kk'}\, |l\rangle\langle l'| \otimes |k\rangle\langle k'|\, \mathrm{e}^{\mathrm{i}(l'-l)\omega_\mathrm{p} t + \mathrm{i}(\varepsilon_{k'}-\varepsilon_k)t},$$

where $|l\rangle$ and $|k\rangle$ denote a Fock state of the plasmon with occupancy l and a momentum state of the electron with wave vector k, respectively. Plugging this expression into eq. (2), we find the explicit differential equations

$$\begin{aligned}\frac{d\alpha_{ll',kk'}}{dt} = {}& \frac{\mathrm{i}g(t)}{\hbar}\big[\alpha_{ll'+1,kk'}\sqrt{l'+1}\mathrm{e}^{\mathrm{i}\omega_\mathrm{p}t} + \alpha_{ll'-1,kk'}\sqrt{l'}\mathrm{e}^{-\mathrm{i}\omega_\mathrm{p}t} \\ & - \alpha_{l+1l',kk'}\sqrt{l+1}\mathrm{e}^{-\mathrm{i}\omega_\mathrm{p}t} - \alpha_{l-1l',kk'}\sqrt{l}\mathrm{e}^{\mathrm{i}\omega_\mathrm{p}t}\big] \\ & + \frac{\gamma}{2}\left[2\sqrt{(l+1)(l'+1)}\alpha_{l+1l'+1,kk'} - (l+l')\alpha_{ll',kk'}\right] \\ & + \frac{\mathrm{i}}{\hbar}\sum_{k''}\big[g^*_{k'k''}\,\alpha_{ll'+1,kk''}\sqrt{l'+1}\,\mathrm{e}^{\mathrm{i}(\varepsilon_{k''}-\varepsilon_{k'}+\omega_\mathrm{p})t} \\ & \quad + g_{k''k'}\,\alpha_{ll'-1,kk''}\sqrt{l'}\,\mathrm{e}^{\mathrm{i}(\varepsilon_{k''}-\varepsilon_{k'}-\omega_\mathrm{p})t} \\ & \quad - g_{kk''}\,\alpha_{l+1l',k''k'}\sqrt{l+1}\,\mathrm{e}^{\mathrm{i}(\varepsilon_k-\varepsilon_{k''}-\omega_\mathrm{p})t} \\ & \quad - g^*_{k''k}\,\alpha_{l-1l',k''k'}\sqrt{l}\,\mathrm{e}^{\mathrm{i}(\varepsilon_k-\varepsilon_{k''}+\omega_\mathrm{p})t}\big] \end{aligned} \quad (3)$$

for the evolution of the density matrix coefficients, which readily leads to the hermiticity condition $\alpha_{ll',kk'} = (\alpha_{l'l,k'k})^*$.

We solve eq. (3) perturbatively in the electron-plasmon interaction, but to all orders in the light-plasmon interaction, so that we decompose $\alpha = \alpha^{(0)} + \alpha^{(1)} + \cdots$, where the terms $\alpha^{(m)}$ have an m-order dependence on the coefficients $g_{kk'}$. In this scheme, as explained for example in Ref. (26), the density matrix to zeroth order in the electron-plasmon interaction (i.e., in the infinite past) reads

$$\rho^{(0)} = |k_0\rangle\langle k_0| \otimes |\xi\rangle\langle\xi|, \quad (4)$$

where k_0 is the wave vector of the incident electron, while $|\xi\rangle = \mathrm{e}^{-|\xi|^2/2}\sum_{l=0}^\infty (\xi^l/\sqrt{l!})\mathrm{e}^{-\mathrm{i}l\omega_\mathrm{p}t}|l\rangle$ is a coherent plasmon state characterized by the time-dependent amplitude

$$\begin{aligned}\xi &= \frac{-\mathrm{i}}{\hbar}\int_{-\infty}^{t} dt'\, g(t')\mathrm{e}^{\mathrm{i}\omega_\mathrm{p}t' - \gamma(t-t')/2} \\ &= \frac{-1}{\hbar}\left[\frac{g_0\mathrm{e}^{\mathrm{i}(\omega_\mathrm{p}-\omega_0)t}}{\omega_\mathrm{p}-\omega_0-\mathrm{i}\gamma/2} + \frac{g_0^*\mathrm{e}^{\mathrm{i}(\omega_\mathrm{p}+\omega_0)t}}{\omega_\mathrm{p}+\omega_0-\mathrm{i}\gamma/2}\right]. \end{aligned} \quad (5)$$

We note that this state corresponds to a number of optically-excited plasmons given by $n = |\xi|^2$. Under the approximations $|\omega_\mathrm{p} + \omega_0| \gg \gamma$ (narrow width) and $|\omega_\mathrm{p} - \omega_0| \ll \gamma$ (resonant excitation), we find $n \approx |2g_0/\hbar\gamma|^2$.

Using eqs. (4) and (5), we can readily write the unperturbed (from the electron-plasmon-interaction viewpoint) coefficients of the density matrix as

$$\alpha^{(0)}_{ll',kk'} = \delta_{kk_0}\delta_{k'k_0}\mathrm{e}^{-|\xi|^2}\frac{\xi^l(\xi^{l'})^*}{\sqrt{l!l'!}}.$$

We assume this value of the coefficients at an initial time $t = t_0$ and integrate eq. (3) by retaining terms of the same order on both sides of the equation, so that $\alpha^{(m)}$ for each order m is obtained from the coefficients for orders $< m$. Repeating this procedure twice (to first obtain $\alpha^{(1)}$ from $\alpha^{(0)}$, and then $\alpha^{(2)}$ from $\alpha^{(1)}$), and integrating up to a time t such that $\gamma(t - t_0) \gg 1$, we calculate the electron transition rate to the lowest nonvanishing order in the electron-plasmon interaction as

$$P_k = \lim_{t-t_0\gg 1/\gamma}\sum_l \frac{\alpha^{(2)}_{ll,kk}}{t-t_0}.$$

This expression gives the population (i.e., the diagonal elements of the density matrix) of states in which the electron has evolved to a new wave vector k, with the plasmons traced out.

For a dipole-like plasmon (e.g., the dipolar mode of a metallic sphere, or also a dipolar mode in one of the silver cubes under consideration), the electron-plasmon interaction coefficient can be obtained from the electric field produced by the electron acting on the plasmon dipole $\mathbf{p}$. We find (27)

$$g_{kk'} = \frac{2e}{\gamma_r^2 L}\,\mathbf{p}\cdot[|q|\gamma_r K_1(|q|R/\gamma_r)\hat{\mathbf{R}} - \mathrm{i}qK_0)(|q|R/\gamma_r)\hat{\mathbf{z}}],$$

where $q = k - k'$, v is the electron velocity, $\gamma_r = 1/\sqrt{1 - v^2/c^2}$ accounts for relativistic corrections, R is the distance from the dipole to the electron trajectory, and L is a quantization length along the beam direction. This expression assumes the non-recoil approximation, in which the electron velocity is taken to remain nearly unchanged during interaction with the plasmon under the assumption $|k-k_0| \ll k_0$, which directly implies $\omega \approx (k-k_0)v$ from energy and momentum conservation. Multiplying the transition rate P_k by the interaction time L/v and using the conversion $\sum_k \to (L/2\pi)\int d\omega$, we finally obtain the electron spectrum

$$\Gamma(\omega) = \frac{L^2}{2\pi v} P_k,$$

where the L^2 factor correctly cancels the $1/L$ dependence of the $g_{kk'}$ coupling coefficients to $m = 2$ order in the calculation of P_k. Nevertheless, for the present discussion, the magnitude of the coupling coefficient $g_{kk'}$ is essentially absorbed in an overall constant in the resulting electron spectral intensity.

We present characteristic examples of calculation in Figure 8 for different values of the light frequency ω_0 (vertical axis) relative to the plasmon frequency ω_p in a regime of weak interaction between the electron and the plasmon (i.e., a regime in which the ZLP is not substantially depleted by loss and gain events). In these calculations, the illumination intensity is expressed in terms of the parameter $n = |2g_0/\hbar\gamma|^2$ (i.e., the population of the plasmon mode), which we take to be independent of ω_0 for the sake of this analysis, although in practice this parameter should follow a Lorentzian profile as the light frequency is swept across the plasmon resonance. We observe an illumination-independent conventional EELS feature in the loss part of the spectrum corresponding to a plasmon with a broadening determined by the parameter γ ($= 0.3\omega_\mathrm{p}$ in the present case), accompanied by symmetric narrow peaks originating in stimulated loss and gain at frequencies $\omega = \pm\omega_0$ relative to the ZLP. In contrast to the broad spontaneous EELS feature, the width of the stimulated peaks is roughly inversely proportional to $1/(t - t_0)$, with the simulation time t taken here to be $t - t_0 = 100/\gamma$. We thus observe a spectrum consisting of a regular EELS spectrum (independent of illumination), on which narrow sEELS and sEEGS peaks are superimposed. This result is in good agreement with the experiment, keeping in mind that stimulated peaks are broadened by the ZLP width and, to a smaller extend, by the laser linewidth. It can be understood in terms of energy conservation because stimulated processes involve discrete energy transfers between electrons and photons mediated by the plasmon. Also, the lack of interference between regular EELS and sEELS is consistent with the fact that they are associated with mutually incoherent processes. Finally, the integral of the signal in the plots of Figure 8 for $\omega > 0$ (loss) and $\omega < 0$ (gain) is approximately given, within the numerical uncertainty, by $(n + 1)/n$, so the conclusion extracted above in the absence of losses is still maintained, although the spectral distribution of the n and $+1$ terms follow different characteristics.

5. Conclusion

We have presented an alternative solution for performing sEELS/sEEGS experiments. In our approach, we use a nanosecond laser instead of a femtosecond laser, and the electron detection rather than the electron excitation is pulsed. sEELS/sEEGS signals could be unambiguously detected. Although they resemble those obtained with a pulsed excitation, the coupling efficiency is much smaller, and most of the phenomena can be understood in a perturbative manner. This configuration allows us to genuinely switch from a normal EELS operation mode to sEELS/sEEGS operation mode with comparable energy resolution. It also makes it easier to perform spectral imaging. Indeed, we report two-dimensional spectral images acquired with a sEELS/sEEGS signal. It allows us to accurately study scenarios in which the excitation is in resonance with a particular plasmon of the sample. Under such circumstances, both EELS and EEGS signals are amplified. However, the EELS signal is larger and its ratio to the EEGS signal given by $sEELS/sEEGS = \frac{n+1}{n}$, where n is the average number of light-induced plasmons. This is because the EELS signal is an incoherent superposition of the spontaneous and stimulated EEL events. In order to describe these phenomena, the plasmon decay which is usually not included in EEGS theory, has been introduced in a new theoretical approach.

The versatility of the setup should allow its direct implementation in any modern microscope, thus gives us some hope that sEELS/sEEGS physics will be more widely studied in the coming years. In particular, the

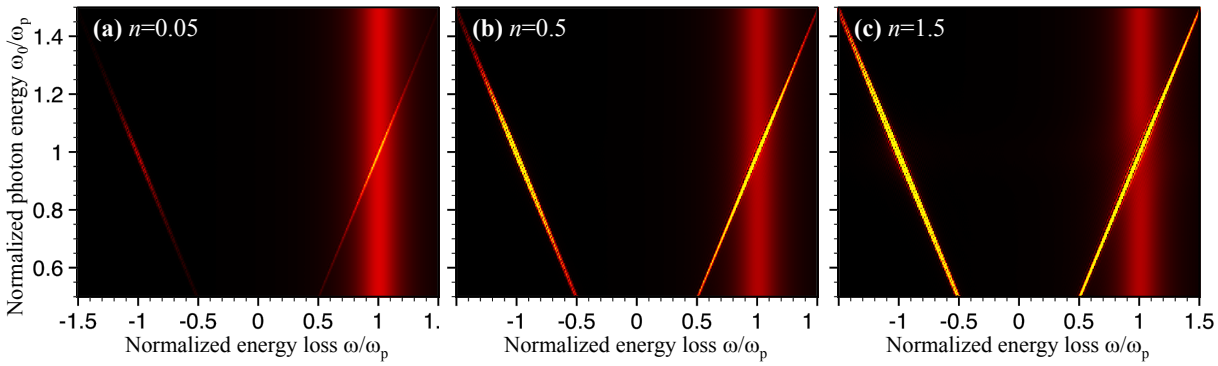

Figure 8: Calculated spectra for interaction of an electron beam with an illuminated plasmon mode, as described in the formalism presented in the main text. We present the evolution of spectra for different values of the light frequency ω_0. The loss and light frequencies (horizontal and vertical axes, respectively) are both normalized to the plasmon frequency ω_p. The plasmon width is assumed to be $\gamma = 0.3\omega_p$. The plasmon-light interaction strength is quantified in terms of the parameter mean number of plasmons $n = |2g_0/\hbar\gamma|^2$ (see labels).

study of resonant effects, first demonstrated here at one particular excitation wavelength, should be straightforwardly extended using tunable lasers. Spectroscopy with spectral resolution only limited by the energy width of the laser, which is orders of magnitude better than the ZLP width, would then be possible by studying the laser wavelength dependence of the sEELS/sEEGS peaks (13; 27).

6. Acknowledgments

MK wants to thank F. Houdellier and A. Arbouet for fruitful discussions. This work has received support from the National Agency for Research under the program of future investment TEMPOS-CHROMATEM with the Reference No. ANR-10-EQPX-50 and FEMTOTEM ANR-14-CE26-0013. FJGA acknowledges support from ERC (Advanced Grant 789104-eNANO) and the Spanish MINECO (MAT2017-88492-R and SEV2015-0522). LFZ and YA acknowledges support from FAPESP (grants 2014/23399-9 and 2017/00259-5).

[1] A. Howie, Electrons and photons: exploiting the connection, in: Inst. Phys. Conf. Ser, Vol. 161, 1999, pp. 311–314.

[2] L. H. G. Tizei, M. Kociak, Spatially resolved quantum nano-optics of single photons using an electron microscope, Physical Review Letters 110 (15) (2013) 153604. doi:10.1103/PhysRevLett.110.153604.

[3] R. Bourrellier, S. Meuret, A. Tararan, O. Stéphan, M. Kociak, L. H. G. Tizei, A. Zobelli, Bright uv single photon emission at point defects in h-bn, Nano Letters 16 (7) (2016) 4317–4321, pMID: 27299915.

[4] L. Douillard, F. Charra, Z. Korczak, R. Bachelot, S. Kostcheev, G. Lerondel, P. M. Adam, P. Royer, Short range plasmon resonators probed by photoemission electron microscopy, Nano Letters 8 (3) (2008) 935–940.

[5] A. Losquin, T. T. Lummen, Electron microscopy methods for space-, energy-, and time-resolved plasmonics, Frontiers of Physics 12 (1) (2017) 127301.

[6] A. Kubo, N. Pontius, H. Petek, Femtosecond microscopy of surface plasmon polariton wave packet evolution at the silver/vacuum interface, Nano letters 7 (2) (2007) 470–475.

[7] R. Zhang, Y. Zhang, Z. Dong, S. Jiang, C. Zhang, L. Chen, L. Zhang, Y. Liao, J. Aizpurua, Y. e. Luo, et al., Chemical mapping of a single molecule by plasmon-enhanced raman scattering, Nature 498 (7452) (2013) 82.

[8] H. Boersch, J. Geiger, W. Stickel, Interaction of 25-kev electrons with lattice vibrations in lif. experimental evidence for surface modes of lattice vibration, Physical Review Letters 17 (7) (1966) 379.

[9] H. Ibach, Optical surface phonons in zinc oxide detected by slow-electron spectroscopy, Phys. Rev. Lett. 24 (25) (1970) 1416–1418.

[10] M. J. Lagos, A. Trügler, U. Hohenester, P. E. Batson, Mapping vibrational surface and bulk modes in a single nanocube, Nature 543 (7646) (2017) 529–532.
URL http://dx.doi.org/10.1038/nature21699

[11] J. Schilling, H. Raether, Energy gain of fast electrons interacting with surface plasmons, Journal of Physics C: Solid State Physics 6 (18) (1973) L358.

[12] J. A. Edighoffer, W. D. Kimura, R. H. Pantell, M. A. Piestrup, D. Y. Wang, Observation of inverse Čerenkov interaction between free electrons and laser light, Phys. Rev. A 23 (1981) 1848–1854. doi:10.1103/PhysRevA.23.1848.
URL https://link.aps.org/doi/10.1103/PhysRevA.23.1848

[13] F. J. G. de Abajo, M. Kociak, Electron energy-gain spectroscopy, New Journal Of Physics 10 (2008) 073035.

[14] B. Barwick, D. J. Flannigan, A. H. Zewail, Photon-induced near-field electron microscopy, Nature 462 (7275) (2009) 902–906.

[15] F. J. G. de Abajo, A. Asenjo-Garcia, M. Kociak, Multiphoton absorption and emission by interaction of swift electrons with evanescent light fields, Nano Letters 10 (5) (2010) 1859–1863.

[16] L. Piazza, T. T. A. Lummen, E. Q. n. onez, Y. Murooka, B. W. Reed, B. Barwick, F. Carbone, Simultaneous observation of the quantization and the interference pattern of a plasmonic near-field, Nature Communications 6 (2015) 1–7.

[17] E. Pomarico, I. Madan, G. Berruto, G. M. Vanacore, K. Wang, I. Kaminer, F. J. García de Abajo, F. Carbone, mev resolution in laser-assisted energy-filtered transmission electron microscopy, ACS Photonics 5 (3) (2017) 759–764.

[18] A. Feist, K. E. Echternkamp, J. Schauss, S. V. Yalunin, S. Schaefer, C. Ropers, Quantum coherent optical phase modulation in an ultrafast transmission electron microscope, Nature 521 (7551) (2015) 200–+. doi:10.1038/nature14463.

[19] G. M. Vanacore, I. Madan, G. Berruto, K. Wang, E. Pomarico, R. J. Lamb, D. McGrouther, I. Kaminer, B. Barwick, F. J. G. de Abajo, F. Carbone, Attosecond coherent control of free-electron wave functions using semi-infinite light fields, Nature Communications (2018) 1–11.

[20] A. Arbouet, G. Caruso, F. Houdellier, Review in Adv. Imag. And Elec. Phys. 207.

[21] F. Houdellier, G. M. Caruso, S. Weber, M. Kociak, A. Arbouet, Development of a high brightness ultrafast Transmission Electron Microscope based on a laser-driven cold field emission source, Ultramicroscopy 186 (2018) 128–138.

[22] A. Campos, N. Troc, E. Cottancin, M. Pellarin, H.-C. Weissker, J. Lermé, M. Kociak, M. Hillenkamp, Plasmonic quantum size effects in silver nanoparticles are dominated by interfaces and local environments, Nat Phys 111 (2018) 1.

[23] A. Feist, N. Bach, N. R. da Silva, T. Danz, M. Möller, K. E. Priebe, T. Domröse, J. G. Gatzmann, S. Rost, J. Schauss, et al., Ultrafast transmission electron microscopy using a laser-driven field emitter: Femtosecond resolution with a high coherence electron beam, Ultramicroscopy 176 (2017) 63–73.

[24] O. L. Krivanek, T. C. Lovejoy, N. Dellby, T. Aoki, R. W. Carpenter, P. Rez, E. Soignard, J. Zhu, P. E. Batson, M. J. Lagos, R. F. Egerton, P. A. Crozier, Vibrational spectroscopy in the electron microscope, Nature 514 (7521) (2014) 209–212.

[25] M. Kociak, O. Stephan, Mapping plasmons at the nanometer scale in an electron microscope, Chem. Soc. Rev. 43 (2014) 3865–3883. doi:10.1039/C3CS60478K.
URL http://dx.doi.org/10.1039/C3CS60478K

[26] F. J. García de Abajo, Multiple excitation of confined graphene plasmons by single free electrons, ACS Nano 7 (2013) 11409–11419.

[27] A. Asenjo-Garcia, F. J. García de Abajo, Plasmon electron energy-gain spectroscopy, New J. Phys. 15 (2013) 103021.